PHILOSOPHICAL TRANSACTIONS A

royalsocietypublishing.org/journal/rsta

Research

Cite this article: Carta G, Colquitt DJ, Movchan AB, Movchan NV, Jones IS. 2019 One-way interfacial waves in a flexural plate with chiral double resonators. *Phil. Trans. R. Soc. A* **378**: 20190350.
http://dx.doi.org/10.1098/rsta.2019.0350

Accepted: 2 October 2019

One contribution of 12 to a theme issue 'Modelling of dynamic phenomena and localization in structured media (part 2)'.

Subject Areas:
applied mathematics, mechanics, structural engineering

Keywords:
flexural waves, chirality, gyroscopic spinners, one-way interfacial waves, double resonators

Author for correspondence:
G. Carta
e-mail: giorgio.carta@liverpool.ac.uk

Electronic supplementary material is available online at https://doi.org/10.6084/m9.figshare.c.4698296.

THE ROYAL SOCIETY PUBLISHING

One-way interfacial waves in a flexural plate with chiral double resonators

G. Carta[1], D. J. Colquitt[1], A. B. Movchan[1], N. V. Movchan[1] and I. S. Jones[2]

[1]Department of Mathematical Sciences, University of Liverpool, Liverpool L69 7ZL, UK
[2]Mechanical Engineering and Materials Research Centre, Liverpool John Moores University, Liverpool L3 3AF, UK

GC, 0000-0003-1325-8070; ABM, 0000-0001-8902-9923

In this paper, we demonstrate a new approach to control flexural elastic waves in a structured chiral plate. The main focus is on creating one-way interfacial wave propagation at a given frequency by employing double resonators in a doubly periodic flexural system. The resonators consist of two beams attached to gyroscopic spinners, which act to couple flexural and rotational deformations, hence inducing chirality in the system. We show that this elastic structure supports one-way flexural waves, localized at an interface separating two sub-domains with gyroscopes spinning in opposite directions, but with otherwise identical properties. We demonstrate that a special feature of double resonators is in the directional control of wave propagation by varying the value of the gyricity, while keeping the frequency of the external time-harmonic excitation fixed. Conversely, for the same value of gyricity, the direction of wave propagation can be reversed by tuning the frequency of the external excitation.

This article is part of the theme issue 'Modelling of dynamic phenomena and localization in structured media (part 2)'.

1. Introduction

Bloch–Floquet waves in periodic systems are generally dispersive and may show interesting behaviour, such as dynamic anisotropy and localization in different

frequency regimes. In addition, waves in lattices having defects of a semi-infinite extent (such as cracks, for example) bring additional analytical and numerical challenges.

An elegant analytical approach to study cracks in lattices was developed by Slepyan [1], where the model is reduced to the analysis of a functional equation (or a system of functional equations) of the Wiener–Hopf type, whose kernel incorporates information about dispersion properties of the Bloch–Floquet waves in the periodic system. Quasi-static and dynamic problems for cracks in different types of media, both linear and nonlinear, were investigated in depth by Slepyan in [1–3] (see also [4–6]). In particular, the specified direction of crack propagation brings a natural directional preference into the problem, and waves emanated from the crack tip may have different physical features ahead of the crack and behind the crack front.

Directional preference and dynamic anisotropy for waves in lattice systems were studied in [7,8]. Chiral systems bring new features complementing dynamic anisotropy with the special property of one-way wave propagation. In the present paper, we analyse directional preference phenomena for the case of a doubly periodic system of specially designed resonators, made of elastic beams and gyroscopic spinners, connected to a Kirchhoff elastic plate. The chiral nature of gyroscopic resonators enables us to break the symmetry and to form 'one-way waveforms' along interfaces. This unusual dynamic response of the structured elastic system is connected to the novel dispersion properties of Bloch–Floquet waves supported by the corresponding doubly periodic chiral systems, as discussed in the main text of the paper.

The concept of gyrobeams, developed in [9–12], highlights interesting features of elongated flexural elastic systems, which include active chirality and a special type of coupling between transverse displacements associated with flexural deformations. We note that active chirality is qualitatively different from geometrically chiral passive systems, also discussed in the literature (see [13–18]).

Recent papers [19,20] have demonstrated that gyrobeams can be understood in the context of homogenization approximations for elongated elastic solids containing multiple spinners connected along the axis of the solid. Although the classical models of gyroscopic conservative systems (see [21]) are commonly used in engineering practice, additional novel spectral properties have been studied for elastic systems including gyroscopic spinners, in the context of the theory of elastic waves in chiral metamaterials [22–25].

The present paper addresses new features in the dynamic response of gyroscopic systems with resonators that incorporate more than one spinner. The spectral problem for a beam with several spinners can be solved analytically in the linear approximation framework [26]. This provides a rich range of options to control vibrations of such systems by changing the gyricities of the spinners. The term gyricity was introduced in [19,20] to characterize the gyroscopic action of individual spinners. If an elastic flexural plate is attached to a doubly periodic array of such resonators, an interface can be created by changing the sign of the gyricity in a sub-domain of the plate. Appropriate choice of the forcing frequency will lead to the generation of a one-way waveform, as shown in figure 1. Furthermore, the direction of wave propagation can be reversed by the appropriate tuning of the gyricity of the spinners. Changing the direction of wave propagation is not possible in a plate containing single-spinner resonators, investigated in [27].

The new work presented here delivers results which are substantially different from elastic periodic systems without chiral resonators (see [28,29]). In particular, the latter systems do not break time-reversal symmetry, which is the fundamental feature to generate one-way wave propagation.

One-way unidirectional waves immune to backscattering were firstly observed in photonic crystals [30–34], motivated by the analogy with the edge states in topological insulators linked to the quantum Hall effect. In elastic and mechanical systems, one-way edge and interfacial waves have been generated in plates [35–38], elastic lattices with spinners [39–41], granular media [42] and systems with coupled pendula [43]. We note that in most of these works, the formation of one-way waveforms has been connected with 'breaking the Dirac cones' of the dispersion surfaces via perturbation of the geometry and physical properties of the periodic system. In the present case of a doubly periodic structure with double-spinner resonators, the mechanism of creating

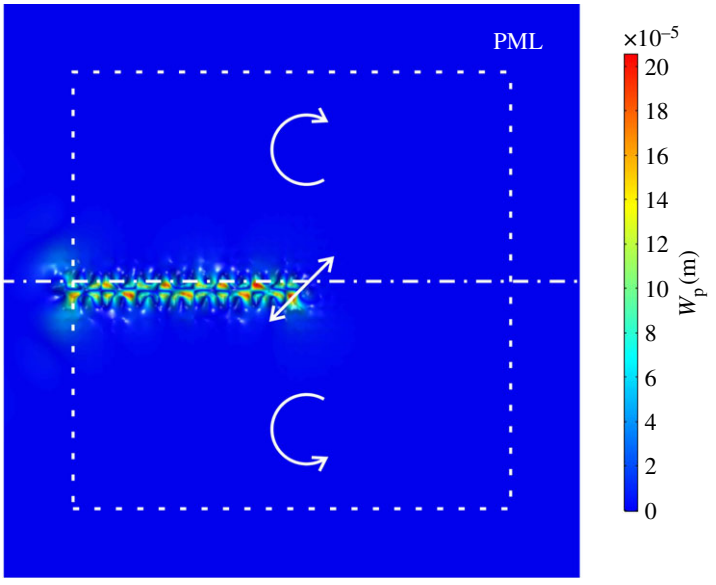

Figure 1. Displacement amplitude field in a plate with a doubly periodic array of chiral double resonators, consisting of two beams with two gyroscopic spinners. The domain is divided into two regions with equal and opposite values of the gyricity of the spinners. A time-harmonic force is imposed on one of the resonators, in the position indicated by the arrow. PML (*Perfectly Matched Layers*) are introduced near the boundaries of the computational domain to avoid wave reflections. (Online version in colour.)

waveforms in the 'time-reversal' mode does not require the presence of broken Dirac cones. The details of the analysis are given in §4.

Localization phenomena in periodic systems have been extensively investigated in the literature. In particular, distributed rotational inertia has been exploited to create localized waveforms in arrays of Rayleigh beams [44–46]. Highly localized waves have been realized in grids of axially and flexurally deformable beams by introducing the effect of pre-stress [47]. Trapping, enhanced transmission and control of flexural waves in thin elastic plates incorporating periodic arrays of different types of resonators have been studied in [29,48–51]. In the present work, the chiral properties of the resonators attached to the plate allow the breakage of time-reversal symmetry of the system and, consequently, lead to the formation of one-way interfacial waves if the domain is split into two regions with different signs of gyricity.

The structure of the paper is as follows. Section 2 includes the formal description of the model and the special example of a spectral problem for an elastic beam connected to two gyroscopic spinners. The eigenvalues are obtained in the closed analytical form, and their dependence on the gyricity of the spinners is discussed in detail. In §3, we analyse Bloch–Floquet waves in a Kirchhoff plate connected to a doubly periodic system of double-spinner resonators. Interfacial waves possessing one-way preferential directionality are constructed and analysed in §4. Concluding remarks and discussion are included in §5.

2. A plate incorporating a chiral flexural double resonator

We study flexural vibrations in a Kirchhoff plate connected to a chiral flexural resonator. As shown in figure 2, the middle plane of the plate lies in the xy-plane and the axis of the resonator is parallel to the z-axis. The resonator consists of two Euler–Bernoulli beams, connected to two gyroscopic spinners at the points B and C. Accordingly, such a resonator will be referred to as a 'double resonator' in the rest of the paper, to distinguish it from the 'single resonator' investigated in [27], represented by a single beam and a gyroscopic spinner at the tip of the beam. As in [20,26],

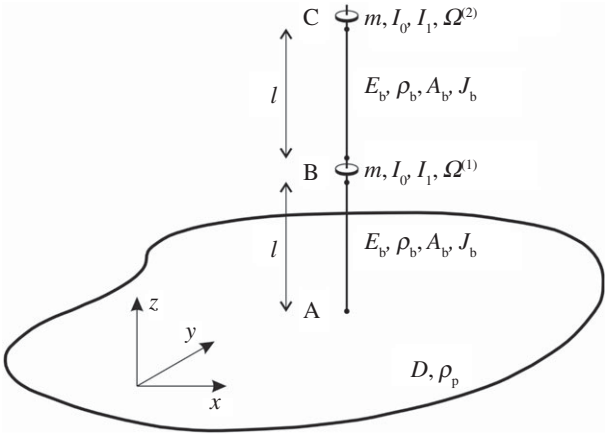

Figure 2. Model of a plate including a chiral flexural double resonator represented by two beams connected to two gyroscopic spinners.

continuity of displacements and flexural rotations is prescribed at the junctions between the beams and the spinners (points B and C in figure 2); in addition, the spinning motions of the gyroscopic spinners are not transmitted to the beams, using the type of connection described in [20]. We also assume that at the junction A, the beam axis always remains orthogonal to the plate.

The equation of motion of the Kirchhoff plate in the time-harmonic regime is given by

$$\Delta^2 W_\mathrm{p} - \beta_\mathrm{p}^4 W_\mathrm{p} = 0, \tag{2.1}$$

where Δ^2 is the biharmonic operator, $W_\mathrm{p} = W_\mathrm{p}(x, y)$ is the amplitude of the plate's transverse displacement in the z-direction, $\beta_\mathrm{p} = (\rho_\mathrm{p} h\omega^2/D)^{1/4}$ is the frequency-like parameter for the plate, ω is the angular frequency, ρ_p is the mass density of the plate, h is the thickness and $D = E_\mathrm{p} h^3/[12(1-\nu_\mathrm{p}^2)]$ is the flexural stiffness of the plate, E_p and ν_p being the Young's modulus and Poisson's ratio of the plate, respectively.

The governing equations of the Euler–Bernoulli beams in the time-harmonic regime are expressed by

$$(U_\mathrm{b}^{(j)})'''' - \beta_b^4 U_\mathrm{b}^{(j)} = 0, \quad (V_\mathrm{b}^{(j)})'''' - \beta_b^4 V_\mathrm{b}^{(j)} = 0 \quad \text{and} \quad E_\mathrm{b}(W_\mathrm{b}^{(j)})'' + \rho_\mathrm{b}\omega^2 W_\mathrm{b}^{(j)} = 0, \tag{2.2}$$

with $j = 1, 2$. In (2.2), the derivatives are taken with respect to z and $U_\mathrm{b}^{(j)} = U_\mathrm{b}^{(j)}(z)$, $V_\mathrm{b}^{(j)} = V_\mathrm{b}^{(j)}(z)$ and $W_\mathrm{b}^{(j)} = W_\mathrm{b}^{(j)}(z)$ $(j = 1, 2)$ are the amplitudes of the transverse and longitudinal displacements of the beams. Further, $\beta_\mathrm{b} = (\rho_\mathrm{b} A_\mathrm{b}\omega^2/(E_\mathrm{b} J_\mathrm{b}))^{1/4}$ is the frequency-like parameter for the beams, E_b and ρ_b are the Young's modulus and mass density of the beams, and A_b and J_b are the beams' cross-sectional area and second moment of inertia, respectively. Here, we assume that the two beams have the same geometrical and material properties. The lengths l of the beams are fixed.

The junction conditions defining the connection between the plate and the beam were derived in [27] and employ the notion of 'logarithmic rotational spring'. The derivation of these junction conditions is presented in appendix A. After imposing continuity of displacements and rotations between the beam and the plate, the beam can be studied on its own, substituting the junction conditions at the connection between the beam and the plate with boundary conditions for the beam. For a circular plate of radius R, clamped at its boundary and connected at its centre

to a beam with circular cross-section of radius $a = \epsilon R$, the boundary conditions at point A are given by

$$\boldsymbol{Y}_{\mathrm{b}}^{(1)}(0) = \boldsymbol{0}, \tag{2.3}$$

$$E_{\mathrm{b}} J_{\mathrm{b}} (\boldsymbol{Y}_{\mathrm{b}}^{(1)})''(0) = -\frac{4\pi D(1+\epsilon^2)}{1-\epsilon^2+(1+\epsilon^2)\log(\epsilon)} (\boldsymbol{Y}_{\mathrm{b}}^{(1)})'(0), \tag{2.4}$$

$$E_{\mathrm{b}} A_{\mathrm{b}} (W_{\mathrm{b}}^{(1)})'(0) = \frac{16\pi D(1-\epsilon^2)}{R^2[(1-\epsilon^2)^2 - 4\epsilon^2 \log^2(\epsilon)]} W_{\mathrm{b}}^{(1)}(0), \tag{2.5}$$

where

$$\boldsymbol{Y}_{\mathrm{b}}^{(j)}(z) = \begin{pmatrix} U_{\mathrm{b}}^{(j)}(z) \\ V_{\mathrm{b}}^{(j)}(z) \end{pmatrix} \quad (j = 1, 2). \tag{2.6}$$

In (2.3), we have taken into account that in a Kirchhoff plate, the in-plane displacement components are assumed to be zero. When $\epsilon = a/R \ll 1$, the conditions (2.4) and (2.5) reduce to

$$E_{\mathrm{b}} J_{\mathrm{b}} (\boldsymbol{Y}_{\mathrm{b}}^{(1)})''(0) = -\frac{4\pi D}{\log(\epsilon)} (\boldsymbol{Y}_{\mathrm{b}}^{(1)})'(0) \tag{2.7}$$

and

$$E_{\mathrm{b}} A_{\mathrm{b}} (W_{\mathrm{b}}^{(1)})'(0) = \frac{16\pi D}{R^2} W_{\mathrm{b}}^{(1)}(0), \tag{2.8}$$

respectively. Since the effect of the boundary becomes negligible when $\epsilon \to 0$, the conditions (2.7) and (2.8) can also be used when the beam is attached to any point of the plate and when the plate has a non-circular shape and other boundary conditions, provided that R is understood as an 'equivalent' radius. In particular, the junction conditions (2.7) and (2.8) can be employed for the elementary cell with quasi-periodicity boundary conditions, analysed in §3.

Each gyroscopic spinner is characterized by mass m, moment of inertia I_1 about its axis of revolution and moments of inertia I_0 about the two axes perpendicular to the axis of revolution and passing through the base of the spinner. We assume that the lengths of the gyroscopic spinners are negligible in comparison with the lengths l of the beams. We indicate by $\Omega^{(1)}$ and $\Omega^{(2)}$ the *gyricities* of the two spinners, which are generally different. As discussed in [19,20], the gyricity Ω of a spinner is given by

$$\Omega = \dot{\phi} + \dot{\psi} = \mathrm{Const}, \tag{2.9}$$

where $\dot{\phi}$ and $\dot{\psi}$ are the precession and spin rates, respectively. According to (2.9), the gyricity remains constant throughout the motion.

At the junction point B, we prescribe continuity of displacements and flexural rotations:

$$\boldsymbol{Y}_{\mathrm{b}}^{(1)}(l) = \boldsymbol{Y}_{\mathrm{b}}^{(2)}(l), \quad W_{\mathrm{b}}^{(1)}(l) = W_{\mathrm{b}}^{(2)}(l) \quad \text{and} \quad (\boldsymbol{Y}_{\mathrm{b}}^{(1)})'(l) = (\boldsymbol{Y}_{\mathrm{b}}^{(2)})'(l). \tag{2.10}$$

According to the formulation developed in [19,20], the effect of the gyroscopic spinners is replaced by the following effective junction conditions, representing the balance of bending moments, shear forces and axial forces:

$$\left.\begin{aligned} &E_{\mathrm{b}} J_{\mathrm{b}} (\boldsymbol{Y}_{\mathrm{b}}^{(1)})''(l) = E_{\mathrm{b}} J_{\mathrm{b}} (\boldsymbol{Y}_{\mathrm{b}}^{(2)})''(l) + \boldsymbol{C}^{(1)} (\boldsymbol{Y}_{\mathrm{b}}^{(1)})'(l), \\ &E_{\mathrm{b}} J_{\mathrm{b}} (\boldsymbol{Y}_{\mathrm{b}}^{(1)})'''(l) = E_{\mathrm{b}} J_{\mathrm{b}} (\boldsymbol{Y}_{\mathrm{b}}^{(2)})'''(l) - m\omega^2 \boldsymbol{Y}_{\mathrm{b}}^{(1)}(l), \\ \text{and} \quad &E_{\mathrm{b}} A_{\mathrm{b}} (W_{\mathrm{b}}^{(1)})'(l) = E_{\mathrm{b}} A_{\mathrm{b}} (W_{\mathrm{b}}^{(2)})'(l) + m\omega^2 W_{\mathrm{b}}^{(1)}(l), \end{aligned}\right\} \tag{2.11}$$

where

$$\boldsymbol{C}^{(j)} = \begin{pmatrix} I_0\omega^2 & -\mathrm{i}\omega I_1 \Omega^{(j)} \\ \mathrm{i}\omega I_1 \Omega^{(j)} & I_0\omega^2 \end{pmatrix} \quad (j = 1, 2). \tag{2.12}$$

At point C, we impose the following effective boundary conditions:

$$\left.\begin{aligned} E_{\mathrm{b}}J_{\mathrm{b}}(\boldsymbol{Y}_{\mathrm{b}}^{(2)})''(2l) &= \boldsymbol{C}^{(2)}(\boldsymbol{Y}_{\mathrm{b}}^{(2)})'(2l),\\ E_{\mathrm{b}}J_{\mathrm{b}}(\boldsymbol{Y}_{\mathrm{b}}^{(2)})'''(2l) &= -m\omega^2\boldsymbol{Y}_{\mathrm{b}}^{(2)}(2l),\\ \text{and}\qquad E_{\mathrm{b}}A_{\mathrm{b}}(W_{\mathrm{b}}^{(2)})'(2l) &= m\omega^2 W_{\mathrm{b}}^{(2)}(2l). \end{aligned}\right\} \tag{2.13}$$

We remark that the matrix $\boldsymbol{C}^{(j)}$ $(j=1,2)$ couples the equations of angular momentum balance when $\Omega^{(j)}\neq 0$.

(a) An auxiliary spectral problem for the double resonator

It is important to note that the boundary conditions (2.4) and (2.5) include ϵ and $\log(\epsilon)$. This reflects on the singular perturbation associated with the junction of the one-dimensional beam and the two-dimensional flexural plate. A simplified approach without the singular perturbation would lead to the boundary conditions corresponding to a fixed hinge. This approach is still useful for predicting one-way wave propagation discussed in §4 and it will be considered in this section.

The plate provides translational and rotational stiffness to the double resonator, thus behaving as a flexural foundation. In the limit case when $\epsilon\to 0$ in (2.4) or in (2.7) and J_{b} is constant, the bending moments at the junction between the plate and the double resonator tend to zero. Accordingly, the conditions (2.4) and (2.7) take the form

$$(\boldsymbol{Y}_{\mathrm{b}}^{(1)})''(0)=0. \tag{2.14}$$

In this situation, the eigenfrequencies and eigenfunctions of the double resonator are determined by solving the differential equations (2.2) with the boundary conditions (2.3), (2.14) and (2.5) (or (2.8)) at A, the junction conditions (2.10) and (2.11) at B, and the boundary conditions (2.13) at C.

We note that the amplitudes of the transverse displacements U_{b} and V_{b} and of the longitudinal displacement W_{b} are decoupled. In the following, we focus attention on the flexural vibrations of the double resonator, associated with U_{b} and V_{b}. In order to obtain a closed-form solution for the eigenfrequencies, we assume that the mass of the beams is negligible in comparison with the mass of the gyroscopic spinners. Consequently, the transverse displacement amplitudes U_{b} and V_{b} are cubic functions in z (see (2.2) when $\rho_{\mathrm{b}}=0$).

When $\Omega^{(1)}=\Omega^{(2)}=\Omega$, the double resonator has 14 non-zero eigenfrequencies, 7 of which are positive while the other 7 are negative and with the same absolute values. The two remaining eigenfrequencies are zero. The relations between the gyricity Ω and the eigenfrequency ω can be written explicitly as

$$\left.\begin{aligned} \Omega_{1,2}(\omega) &= \{72(E_{\mathrm{b}}J_{\mathrm{b}})^3-36(E_{\mathrm{b}}J_{\mathrm{b}})^2L(2I_0+5mL^2)\omega^2-2I_0m^2L^7\omega^6\\ &\quad+E_{\mathrm{b}}J_{\mathrm{b}}[mL^4(54I_0+11mL^2)\omega^4\pm(5184(E_{\mathrm{b}}J_{\mathrm{b}})^4\\ &\quad+11088(E_{\mathrm{b}}J_{\mathrm{b}})^2m^2L^6\omega^4-648E_{\mathrm{b}}J_{\mathrm{b}}m^3L^9\omega^6+25m^4L^{12}\omega^8)^{1/2}]\}/\\ &\quad\{2I_1L[36(E_{\mathrm{b}}J_{\mathrm{b}})^2-27E_{\mathrm{b}}J_{\mathrm{b}}mL^3\omega^2+m^2L^6\omega^4]\omega\},\\ \text{and}\qquad \Omega_{3,4}(\omega) &= \{-72(E_{\mathrm{b}}J_{\mathrm{b}})^3+36(E_{\mathrm{b}}J_{\mathrm{b}})^2L(2I_0+5mL^2)\omega^2+2I_0m^2L^7\omega^6\\ &\quad-E_{\mathrm{b}}J_{\mathrm{b}}[mL^4(54I_0+11mL^2)\omega^4\pm(5184(E_{\mathrm{b}}J_{\mathrm{b}})^4\\ &\quad+11088(E_{\mathrm{b}}J_{\mathrm{b}})^2m^2L^6\omega^4-648E_{\mathrm{b}}J_{\mathrm{b}}m^3L^9\omega^6+25m^4L^{12}\omega^8)^{1/2}]\}/\\ &\quad\{2I_1L[36(E_{\mathrm{b}}J_{\mathrm{b}})^2-27E_{\mathrm{b}}J_{\mathrm{b}}mL^3\omega^2+m^2L^6\omega^4]\omega\}. \end{aligned}\right\} \tag{2.15}$$

The functions $\Omega_k(\omega)$ $(k=1,\ldots,4)$ are plotted in figure 3*b*. For the choice of parameters detailed in the caption of figure 3, the curves intersect at four points on the horizontal axis $\Omega=0$, which represent the double eigenfrequencies for the case when the spinners neither spin nor precess. The curves also intersect when $\Omega\neq 0$; one of these common points is shown in the inset of figure 3*b*.

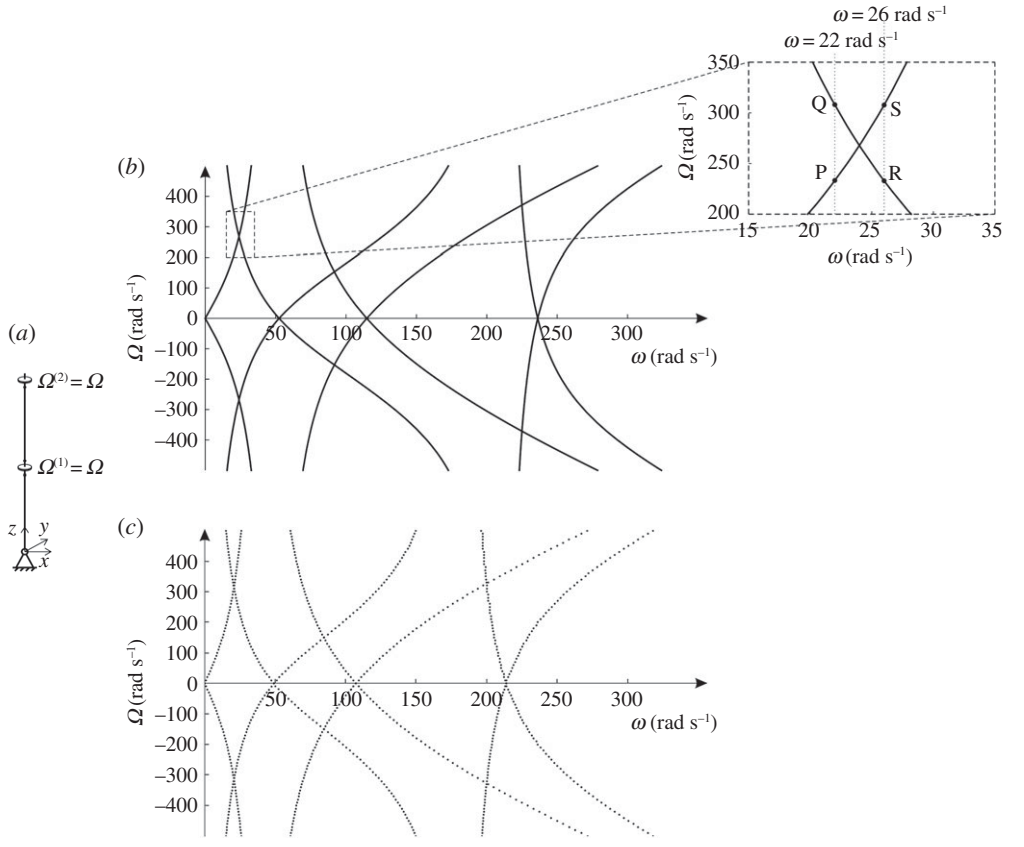

Figure 3. (*a*) Double resonator, hinged at $z = 0$. (*b*) Gyricity Ω versus eigenfrequency ω for the double resonator in (*a*), where the two beams are assumed to be massless ($\rho_b = 0$). The eigenfrequencies are associated with flexural vibrations. The inset shows a magnified view of one of the intersections, including the points where the eigenfunctions are evaluated. (*c*) Gyricity Ω versus eigenfrequency ω in the case when the beams have inertia ($\rho_b = 2700$ kg m^{-3}). In the calculations, we have considered aluminium beams ($E_b = 70$ GPa) of length $l = 1$ m and circular cross-section of radius $a = 0.02$ m, and gyroscopic spinners of mass $m = 5$ kg and moments of inertia $I_0 = 4$ kg m^2 and $I_1 = 2$ kg m^2.

When $\Omega \neq 0$, the eigenfunctions of the double resonator show coupling between flexural and rotational motions. The direction of rotation depends on the curve where the eigenfrequency is computed. As an example, we study the dynamic behaviour of the resonator in the neighbourhood of the intersection displayed in the inset of figure 3*b*. The points P to S have the following values of eigenfrequency and gyricity: $\omega = 22\,\mathrm{rad\,s^{-1}}$ and $\Omega = 233.156\,\mathrm{rad\,s^{-1}}$ at P; $\omega = 22\,\mathrm{rad\,s^{-1}}$ and $\Omega = 307.844\,\mathrm{rad\,s^{-1}}$ at Q; $\omega = 26\,\mathrm{rad\,s^{-1}}$ and $\Omega = 232.958\,\mathrm{rad\,s^{-1}}$ at R; finally, $\omega = 26\,\mathrm{rad\,s^{-1}}$ and $\Omega = 307.685\,\mathrm{rad\,s^{-1}}$ at S. The corresponding eigenfunctions are illustrated in electronic supplementary material, videos S1–S4. It can be seen that at the eigenfrequencies P and S, the resonator rotates in the counter-clockwise direction in the *xy*-plane, while at the eigenfrequencies Q and R, it rotates in the clockwise direction.

Figure 3*b* shows that the same eigenfrequency can be obtained with two different values of gyricity, and the corresponding modes of vibration are characterized by opposite directions of rotation. This result will be exploited in §4 to change the direction of one-way wave propagation, while keeping the frequency of the time-harmonic excitation constant.

Figure 3c illustrates how gyricity varies with angular frequency when the beams possess inertia. In particular, it is assumed that their density is $\rho_b = 2700\,\mathrm{kg\,m^{-3}}$. Figure 3*c* was obtained with a finite-element model built in *Comsol Multiphysics* (v. 5.3). The main effect of adding distributed inertia to the beams is to move the curves to lower values of ω. However, this effect is

not significant in the range of frequencies displayed in figure 3*c*, for the choice of parameters considered here. Accordingly, the simplified model discussed in this section gives important insight into the dynamic behaviour of the double resonator at low frequencies, even when the beams have distributed mass.

3. Doubly periodic array of double resonators attached to a plate

In this section, we study the propagation of Bloch–Floquet flexural waves in an infinite plate connected to a doubly periodic array of double resonators, described in §2. The double resonators are arranged in a square pattern, where the side length of the elementary cell is denoted by L (figure 4). The position of each resonator is defined by the vector $\boldsymbol{r}_{nm} = (nL, mL)$, where $n, m \in \mathbb{Z}$.

In the elementary cell $\mathbf{x} = (x, y) \in (-L/2, L/2) \times (-L/2, L/2)$, the governing equation for the plate's displacement amplitude is given by

$$D\Delta^2 W_\mathrm{p} - \rho_\mathrm{p} h\omega^2 W_\mathrm{p} - N_z(0,\omega)\delta(\mathbf{x}) + M_x(0,\omega)\frac{\partial}{\partial y}\delta(\mathbf{x}) - M_y(0,\omega)\frac{\partial}{\partial x}\delta(\mathbf{x}) = 0, \tag{3.1}$$

where $N_z(z,\omega)$, $M_x(z,\omega)$ and $M_y(z,\omega)$ represent the axial force and bending moments transmitted by the beam, and $\delta(\mathbf{x})$ is the Dirac delta function. Bloch–Floquet quasi-periodicity conditions relate the displacements and rotations at the junctions between the plate and the double resonators:

$$\left.\begin{aligned} &W_\mathrm{p}|_{x=nL,y=mL} = W_\mathrm{p}|_{x=0,y=0}\, \mathrm{e}^{\mathrm{i}\mathbf{k}\cdot\boldsymbol{r}_{nm}}, \\ \text{and}\quad &\nabla W_\mathrm{p}|_{x=nL,y=mL} = \nabla W_\mathrm{p}|_{x=0,y=0}\, \mathrm{e}^{\mathrm{i}\mathbf{k}\cdot\boldsymbol{r}_{nm}}, \end{aligned}\right\} \tag{3.2}$$

where $\boldsymbol{k} = (k_x, k_y)^\mathrm{T}$ is the wavevector. Non-trivial solutions of (3.1) and (3.2) lead to the dispersion relation for the periodic system, which shows how the angular frequency ω depends on the wavevector $\boldsymbol{k}$.

The analytical approach formulated above has been described in detail in [27]. It has also been demonstrated in [27] that the boundary conditions (2.4) and (2.5) produce equivalent results to the numerical computations performed in *Comsol Multiphysics*, for the case of massless plate and beams and of a single spinner per beam.

Here, the dispersion diagrams are determined numerically with a bespoke finite-element model developed in *Comsol Multiphysics*. The governing equation of the plate is given by (2.1) and the rod is modelled as an Euler–Bernoulli beam. In the finite-element model the singular perturbation based on the small parameter ϵ is not used, and the connection between the two-dimensional plate and the one-dimensional beam incorporates continuity of displacements and rotations. The gyroscopic spinners are modelled implementing the effective junction and boundary conditions (2.10)–(2.13). At the boundaries of the elementary cell, we apply Bloch–Floquet conditions:

$$\left.\begin{aligned} &W_\mathrm{p}|_{x=L/2} = W_\mathrm{p}|_{x=-L/2}\, \mathrm{e}^{\mathrm{i}k_x L}, \quad \left.\frac{\partial W_\mathrm{p}}{\partial y}\right|_{x=L/2} = \left.\frac{\partial W_\mathrm{p}}{\partial y}\right|_{x=-L/2} \mathrm{e}^{\mathrm{i}k_x L}, \\ &M_{xx}|_{x=L/2} = M_{xx}|_{x=-L/2}\, \mathrm{e}^{\mathrm{i}k_x L}, \quad M_{xy}|_{x=L/2} = M_{xy}|_{x=-L/2}\, \mathrm{e}^{\mathrm{i}k_x L}, \\ &V_x|_{x=L/2} = V_x|_{x=-L/2}\, \mathrm{e}^{\mathrm{i}k_x L}, \\ &W_\mathrm{p}|_{y=L/2} = W_\mathrm{p}|_{y=-L/2}\, \mathrm{e}^{\mathrm{i}k_y L}, \quad \left.\frac{\partial W_\mathrm{p}}{\partial x}\right|_{y=L/2} = \left.\frac{\partial W_\mathrm{p}}{\partial x}\right|_{y=-L/2} \mathrm{e}^{\mathrm{i}k_y L}, \\ &M_{yy}|_{y=L/2} = M_{yy}|_{y=-L/2} \mathrm{e}^{\mathrm{i}k_y L}, \quad M_{yx}|_{y=L/2} = M_{yx}|_{y=-L/2}\, \mathrm{e}^{\mathrm{i}k_y L}, \\ \text{and}\quad &V_y|_{y=L/2} = V_y|_{y=-L/2}\, \mathrm{e}^{\mathrm{i}k_y L}, \end{aligned}\right\} \tag{3.3}$$

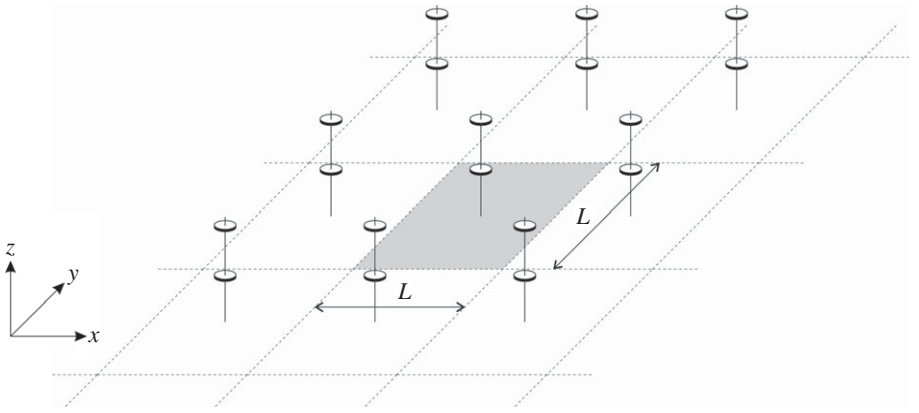

Figure 4. Infinite plate with double resonators arranged in a square array. The elementary cell is highlighted in grey.

where $M_{xx} = -D(W_{\mathrm{p},xx} + \nu W_{\mathrm{p},yy})$, $M_{yy} = -D(W_{\mathrm{p},yy} + \nu W_{\mathrm{p},xx})$, $M_{xy} = M_{yx} = -D(1-\nu)W_{\mathrm{p},xy}$ are the moments and $V_x = M_{xx,x} + M_{xy,y}$, $V_y = M_{yy,y} + M_{yx,x}$ are the shear forces.

In the numerical computations, we consider an aluminium plate with Young's modulus $E_\mathrm{p} = 70\,\mathrm{GPa}$, Poisson's ratio $\nu_\mathrm{p} = 0.3$ and density $\rho_\mathrm{p} = 2700\,\mathrm{kg\,m^{-3}}$. The side length of the square elementary cell is $L = 2\,\mathrm{m}$ and the thickness of the plate is $h = 0.01\,\mathrm{m}$. The beams, which are also made of aluminium, have length $l = 1\,\mathrm{m}$ and a circular cross-section of radius $a = 0.02\,\mathrm{m}$. The gyroscopic spinners have the same gyricity Ω, mass $m = 5\,\mathrm{kg}$ and moments of inertia $I_0 = 4\,\mathrm{kg\,m^2}$ and $I_1 = 2\,\mathrm{kg\,m^2}$.

Figure 5 shows the dispersion diagrams for the periodic system when (a) $\Omega = 0$, (b) close to $\Omega = 200\,\mathrm{rad\,s^{-1}}$ and (c) close to $\Omega = 268.8\,\mathrm{rad\,s^{-1}}$. The dispersion surfaces are presented on the left, while the band diagrams calculated along the path Γ X M Y Γ in the reciprocal space (shown in the insets) are plotted on the right. The band diagrams are symmetric with respect to Γ because the elementary cell is square, even though the structure is chiral. We also note that the number of dispersion surfaces is infinite since the system possesses distributed inertia.

When $\Omega = 0$, namely when the spinners neither spin nor precess, no stop-bands are observed at low frequencies (figure 5*a*). Conversely, when $\Omega \neq 0$ narrow stop-bands are created in the low-frequency regime, as shown in figure 5*b*,*c*. We point out that the value $\Omega = 268.8\,\mathrm{rad\,s^{-1}}$, used in figure 5*c*, has been chosen so that the lower limit of the second stop-band of the corresponding dispersion diagram matches that of the dispersion diagram in figure 5*b*, obtained for $\Omega = 200\,\mathrm{rad\,s^{-1}}$ (see also figure 6). Electronic supplementary material, video S5 presents a comparison of the slowness contours for the three values of Ω considered in figure 5 as the angular frequency ω is varied.

When $\Omega \neq 0$, the flexural vibrations in the plate are coupled with the rotational motion of the double resonators around the z-axis. Electronic supplementary material, videos S6 and S7 show the eigenfunctions of the elementary cell at the point M of the reciprocal space (where $\boldsymbol{k} = (\pi/L, \pi/L)^\mathrm{T}$) and for $\Omega = 200\,\mathrm{rad\,s^{-1}}$, at the frequencies indicated by 'a' and 'b', respectively, in figure 5*b*. These frequencies correspond to the limits of the pass-bands. In electronic supplementary material, video S6, the rotation of the double resonator about the z-axis is counter-clockwise, while in electronic supplementary material, video S7, it is clockwise. This observation is of fundamental importance for the generation of one-way waves, as described in §4. We also point out that the eigenfunctions in electronic supplementary material, videos S6 and S7 are similar, respectively, to those shown in electronic supplementary material, videos S1 and S2, which were determined for a double resonator hinged at the bottom end and made of massless beams.

Electronic supplementary material, videos S8 and S9 show the eigenfunctions of the periodic cell at the frequencies denoted by 'c' and 'd' in figure 5*c*, corresponding to $\Omega =$

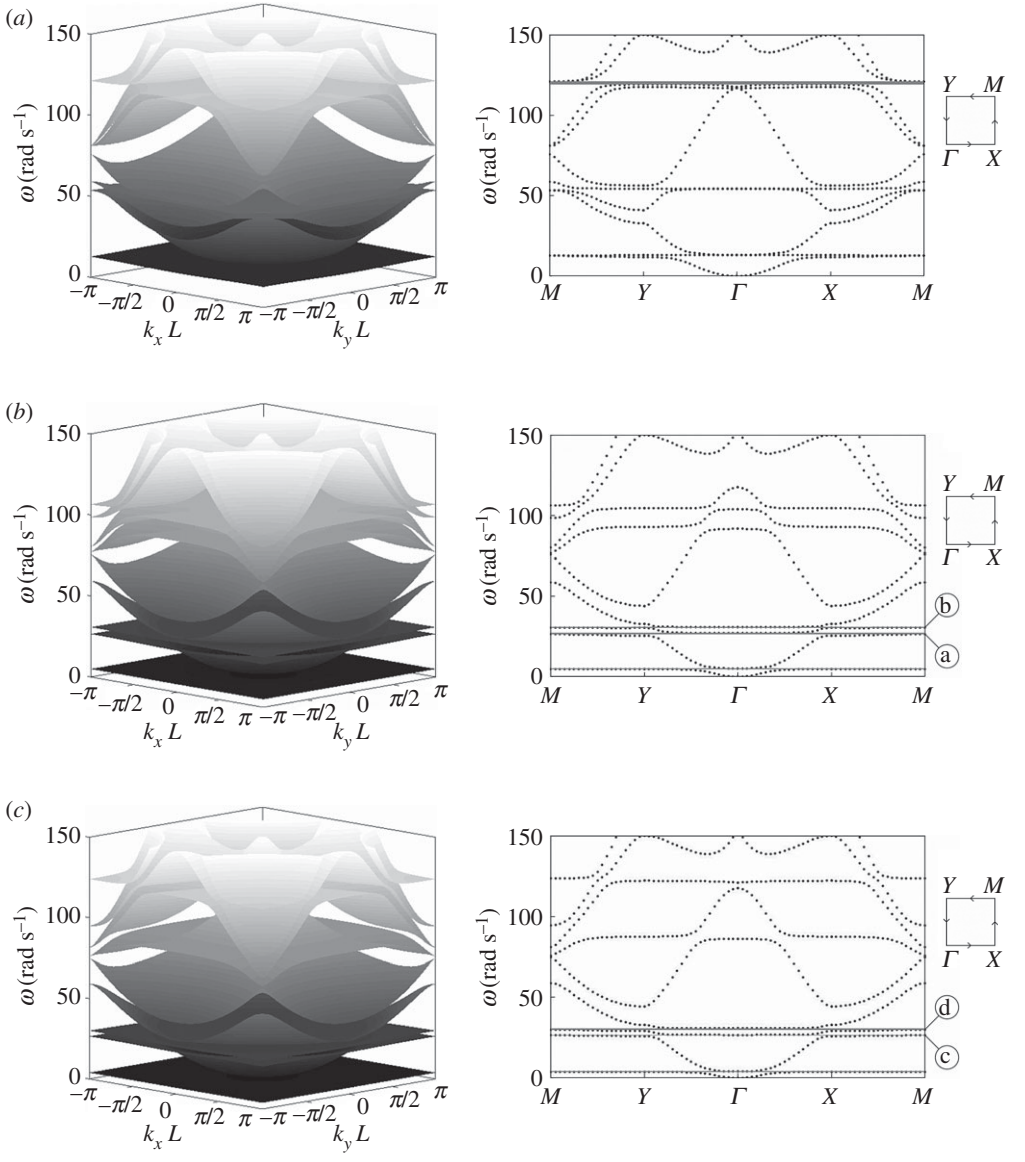

Figure 5. Dispersion surfaces (left) and band diagrams (right) when the gyricity of the spinners is (*a*) $\Omega = 0$, (*b*) $\Omega = 200\ \mathrm{rad\,s^{-1}}$ and (*c*) $\Omega = 268.8\ \mathrm{rad\,s^{-1}}$. The grey regions in the band diagrams represent the stop-bands of the system.

$268.8\ \mathrm{rad\,s^{-1}}$. These videos highlight that the rotation of the double resonator at the lower (higher) frequency is clockwise (counter-clockwise), in contrast to that observed for $\Omega = 200\ \mathrm{rad\,s^{-1}}$. The eigenfunctions in electronic supplementary material, videos S8 and S9 have shapes similar to those in electronic supplementary material, videos S3 and S4, respectively.

Figure 6 shows the eigenfrequencies of the periodic system at point M (where $\boldsymbol{k} = (\pi/L, \pi/L)^{\mathrm{T}}$), calculated for different values of Ω. The direction of rotation of the double resonator remains constant as we move along a single curve. Similar features have been observed with reference to figure 3. The horizontal dashed line indicates the frequency defining the lower limit of the second stop-band for $\Omega = 200\ \mathrm{rad\,s^{-1}}$, which coincides with that corresponding to $\Omega = 268.8\ \mathrm{rad\,s^{-1}}$. However, these frequencies lie on two different lines, that is why the directions of rotation in electronic supplementary material, videos S6 and S8 are opposed though the frequency is identical.

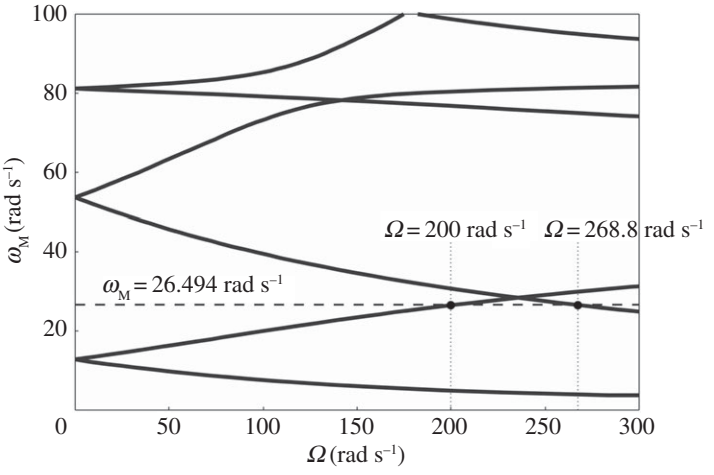

Figure 6. Limits of the pass-bands computed at $\boldsymbol{k} = (\pi/L, \pi/L)^T$ for different values of the gyricity Ω.

The dispersion analysis performed in this section will be useful in predicting the frequencies of external harmonic excitations at which one-way wave propagation will occur, as discussed in the following section.

4. One-way interfacial waves

Gyricity introduces preferential directionality into the system. In the periodic structure studied in §3, the eigenfunctions calculated at the lower and upper limits of a stop-band generally show a different direction of rotation of the double resonators (see, for instance, the eigenfunctions calculated at the points 'a' and 'b' in figure 5*b* and illustrated in electronic supplementary material, videos S6 and S7). Accordingly, gyricity can be exploited to force waves to propagate in one direction, determined by the direction of rotation of the double resonators. When the direction of rotation is changed (refer, for example, to the vibration modes associated with points 'c' and 'd' in figure 5*c* and presented in electronic supplementary material, videos S8 and S9), we expect waves to travel in the opposite direction.

In this section, we consider an infinite structure made of square cells, characterized by the same geometrical and material parameters taken for the periodic cell analysed in §3. In the numerical simulations, the computational domain consist of a plate connected to a 50×50 array of chiral double resonators. A time-harmonic force of amplitude 1 N and parallel to the xy-plane is applied to one resonator, in particular, to the upper gyroscopic spinner. We note that the direction of application of the force is not important. This force generates bending moments, which are transmitted to the plate. Due to the gyroscopic effect, the force produces two bending moments, in both the perpendicular and parallel directions with respect to the direction of the force. PML (*Perfectly Matched Layers*) are inserted at the boundaries of the structure. They are designed as plate elements with damping, whose parameters are tuned in order to minimize reflections of waves from the boundaries (as in [27]).

We start by studying the system shown in figure 7*a*. The domain is divided into two regions, characterized by equal and opposite values of gyricity, as indicated by the circular arrows. In this case, the interface between the two regions is horizontal and straight (see the dot-dashed line in the figure). The force is applied to the upper gyroscopic spinner of the double resonator in the cell highlighted in grey, just below the interface. PML are set at the boundaries of the computational domain.

Using a finite-element model built in *Comsol Multiphysics*, we have determined the response of the chiral structure to the time-harmonic force. In figure 7*b*, we show the displacement

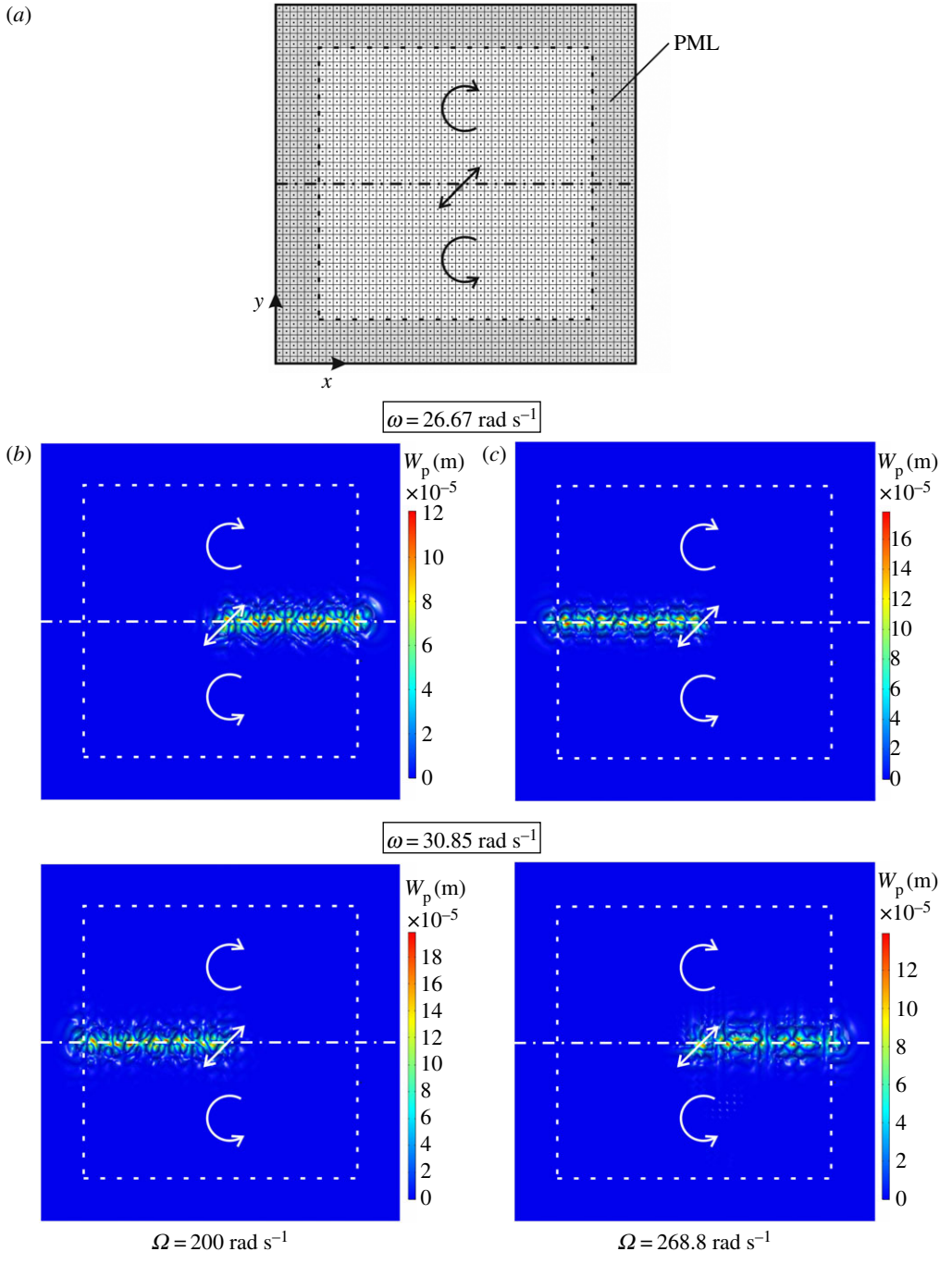

Figure 7. (*a*) Schematic representation of a plate with a 50 × 50 array of double resonators; displacement amplitude fields in the plate when gyricity is (*b*) $\Omega = 200\ \mathrm{rad\ s^{-1}}$ and (*c*) $\Omega = 268.8\ \mathrm{rad\ s^{-1}}$, produced by a time-harmonic force with two different angular frequencies ($\omega = 26.67\ \mathrm{rad\ s^{-1}}$ and $\omega = 30.85\ \mathrm{rad\ s^{-1}}$). (Online version in colour.)

amplitude W_p in the plate when the gyricity is $\Omega = 200\ \mathrm{rad\ s^{-1}}$ and when the angular frequency of the time-harmonic force is $\omega = 26.67\ \mathrm{rad\ s^{-1}}$ (top part) and $\omega = 30.85\ \mathrm{rad\ s^{-1}}$ (bottom part). The frequency $\omega = 26.67\ \mathrm{rad\ s^{-1}}$ falls within the second stop-band of the dispersion diagram for the corresponding periodic system (figure 5*b*), above point 'a'. The frequency $\omega = 30.85\ \mathrm{rad\ s^{-1}}$ is instead located inside the third stop-band, above point 'b'. It is apparent that, in both cases, a

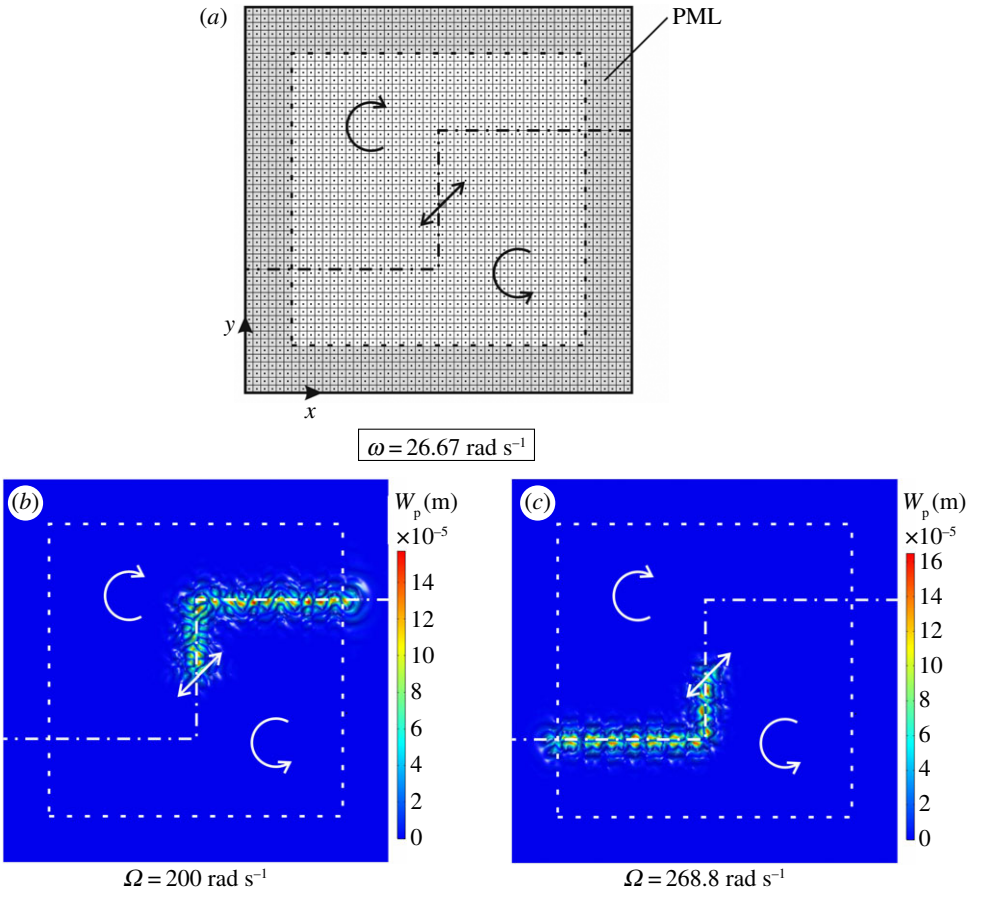

Figure 8. (*a*) Same system as in figure 7*a*, but with a zigzag interface; displacement amplitude fields due to a time-harmonic force of angular frequency $\omega = 26.67\ \mathrm{rad\,s^{-1}}$, when the gyricity is (*b*) $\Omega = 200\ \mathrm{rad\,s^{-1}}$ and (*c*) $\Omega = 268.8\ \mathrm{rad\,s^{-1}}$. (Online version in colour.)

one-way interfacial wave is produced by the excitation. In figure 1, the gyricity was the same ($\Omega = 200\ \mathrm{rad\,s^{-1}}$) and the angular frequency of the external excitation was $\omega = 5.03\ \mathrm{rad\,s^{-1}}$; this frequency lies in the first stop-band of the dispersion diagram of the corresponding periodic system. Figures 1 and 7*b* demonstrate that the direction of wave propagation can be changed by varying the frequency of the external force, while keeping the gyricity the same.

Figure 7*c* presents the contour diagram of the plate's displacement amplitude W_p for the same frequencies ω and for a different value of gyricity, namely $\Omega = 268.8\ \mathrm{rad\,s^{-1}}$. The dispersion diagram for the corresponding periodic system is shown in figure 5*c*. The frequency $\omega = 26.67\ \mathrm{rad\,s^{-1}}$ lies in the second stop-band above point 'c', while $\omega = 30.85\ \mathrm{rad\,s^{-1}}$ falls within the third stop-band above point 'd'. We note that the frequencies $\omega = 26.67\ \mathrm{rad\,s^{-1}}$ and $\omega = 30.85\ \mathrm{rad\,s^{-1}}$ are located in the second and third stop-bands of both dispersion diagrams in figures 5*b*,*c*. This is the reason that one-way interfacial waves are generated for both values of Ω. However, the direction of propagation changes with the gyricity, because the direction of rotation of the double resonators is different for $\Omega = 200\ \mathrm{rad\,s^{-1}}$ and $\Omega = 268.8\ \mathrm{rad\,s^{-1}}$, as discussed in §3 (see also figure 6). Figure 5*b*,*c* demonstrates that the direction of one-way wave propagation can be reversed if the gyricity is changed while the frequency of the external force is kept constant. This may be very important for practical applications.

For a similar structure, an interface has been introduced containing corners as shown in figure 8*a*. Figure 8*b*,*c* presents the fields of transverse displacement amplitude in the plate

when the angular frequency of the external excitation is $\omega = 26.67\,\mathrm{rad\,s^{-1}}$ and the gyricity of the spinners is either $\Omega = 200\,\mathrm{rad\,s^{-1}}$ (figure 8*b*) or $\Omega = 268.8\,\mathrm{rad\,s^{-1}}$ (figure 8*c*). The directions of wave propagation for the two values of gyricity are identical to those shown in figure 7*b*,*c*, respectively. When $\omega = 30.85\,\mathrm{rad\,s^{-1}}$, the direction of propagation is the opposite to that when $\omega = 26.67\,\mathrm{rad\,s^{-1}}$; the results are not given here for brevity. The simulations of figure 8*b*,*c* demonstrate the robustness of interfacial waves. It is also demonstrated how efficiently interfacial waves may be guided around corners with minimal backscattering.

5. Conclusion

In this paper, we have shown that a plate with a doubly periodic array of gyroscopic resonators offers the possibility of creating one-way interfacial waveforms. The dynamic response to an external force can be predicted from the dispersion analysis of the corresponding infinite periodic system, in particular, from the determination of the stop-bands and the analysis of the eigenfunctions at the edges of the pass-bands.

The simulations presented in §4 demonstrate the versatility of the proposed flexural system, where one-way waves can be generated for any frequency of the external excitation by tuning the gyricity and where the direction of propagation can be chosen *ad libitum*, depending on the needs.

The mechanism of creating one-way waveforms does not require breaking Dirac cones. It has also been demonstrated that there is minimal backscattering from the corners along the interfaces.

Although the analysis has been presented for resonators containing two spinners of identical gyricities, the work allows for a significant extension to the case of multiple spinners of different gyricities.

Data accessibility. The paper contains no experimental data. The illustrative computations were performed using *Wolfram Mathematica* (v. 10) and *Comsol Multiphysics* (v. 5.3). All results are directly reproducible.

Authors' contributions. G.C. performed the analytical computations for the double resonator and the numerical computations concerning the two-dimensional band diagrams and the forced problems. D.J.C. carried out the numerical computations for the determination of the dispersion surfaces and the slowness contours. N.V.M. proposed the idea of double chiral resonators. All the authors contributed to the analytical results and to writing the text of the paper.

Competing interests. We declare we have no competing interests.

Funding. The authors would like to thank the EPSRC (UK) for its support through Programme grant no. EP/L024926/1.

Appendix A. Conditions at the junction between the plate and the beam

We consider a circular Kirchhoff plate of radius R, clamped at the boundary and containing a circular rigid inclusion of radius a, as shown in figure 9. We follow the procedure described in [27,52] to derive the relationships between bending moments and rotations and between shear force and transverse displacement at the connection between the plate and the beam, where the latter is modelled by the rigid inclusion.

The conditions at the clamped boundary of the plate are given by

$$W_{\mathrm{p}}|_{r=R} = 0 \quad \text{and} \quad \left.\frac{\partial W_{\mathrm{p}}}{\partial r}\right|_{r=R} = 0. \tag{A 1}$$

We assume that the rigid inclusion is subjected to a time-harmonic displacement of amplitude W_0 in the z-direction and a time-harmonic rotation of amplitude Ψ around the y-axis. Hence, the conditions at the boundary of the inclusion are expressed by

$$W_{\mathrm{p}}|_{r=a} = W_0 - \Psi a\cos(\theta) \quad \text{and} \quad \left.\frac{\partial W_{\mathrm{p}}}{\partial r}\right|_{r=a} = -\Psi\cos(\theta). \tag{A 2}$$

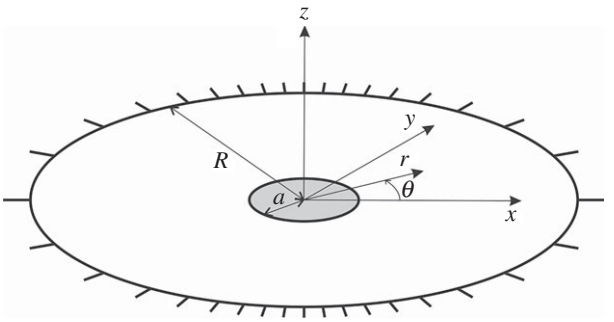

Figure 9. Circular plate clamped at the boundary and including a circular rigid inclusion.

For the sake of simplicity, we assume zero rotation around the x-axis. Of course, the relationship between bending moment and rotation around the x-axis is similar to that derived in the following for the y-axis.

The displacement in the plate, satisfying the governing equation (2.1), has the form

$$W_{\mathrm{p}}(r,\theta) = A_0 J_0(\beta_{\mathrm{p}} r) + B_0 Y_0(\beta_{\mathrm{p}} r) + C_0 I_0(\beta_{\mathrm{p}} r) + D_0 K_0(\beta_{\mathrm{p}} r) + [A_1 J_1(\beta_{\mathrm{p}} r) + B_1 Y_1(\beta_{\mathrm{p}} r) + C_1 I_1(\beta_{\mathrm{p}} r) + D_1 K_1(\beta_{\mathrm{p}} r)]\cos(\theta), \tag{A 3}$$

where $J_n(\beta_{\mathrm{p}} r)$ and $Y_n(\beta_{\mathrm{p}} r)$ $(n = 0, 1)$ are the Bessel functions of the first and second kind, respectively, while $I_n(\beta_{\mathrm{p}} r)$ and $K_n(\beta_{\mathrm{p}} r)$ $(n = 0, 1)$ are the modified Bessel functions of the first and second kind, respectively. The coefficients $A_0, \ldots, D_0$ and $A_1, \ldots, D_1$ are determined from the boundary conditions (A 1) and (A 2).

The shear force V_z and the bending moments M_x and M_y are given by [52]

$$V_z = \int_0^{2\pi} V_r|_{r=a} a \, \mathrm{d}\theta. \tag{A 4}$$

$$M_x = \int_0^{2\pi} (-M_r + V_r a)|_{r=a} \sin(\theta) a \, \mathrm{d}\theta, \tag{A 5}$$

$$M_y = \int_0^{2\pi} (M_r - V_r a)|_{r=a} \cos(\theta) a \, \mathrm{d}\theta, \tag{A 6}$$

where

$$V_r = -D\left[\frac{\partial}{\partial r}(\nabla^2 W_{\mathrm{p}}) + (1-\nu_{\mathrm{p}})\frac{1}{r}\frac{\partial^2}{\partial r \partial \theta}\left(\frac{1}{r}\frac{\partial W_{\mathrm{p}}}{\partial \theta}\right)\right] \tag{A 7}$$

and

$$M_r = -D\left[\nu_{\mathrm{p}} \nabla^2 W_{\mathrm{p}} + (1-\nu_{\mathrm{p}})\frac{\partial^2 W_{\mathrm{p}}}{\partial r^2}\right]. \tag{A 8}$$

We note that in this case $M_x = 0$.

The static limits of V_z and M_y are given by

$$V_z^{\mathrm{static}} = \lim_{\beta_{\mathrm{p}} \to 0} V_z = \frac{16\pi D(a^2 - R^2)}{(a^2 - R^2)^2 - 4a^2 R^2 \log^2(a/R)} W_0 \tag{A 9}$$

and

$$M_y^{\mathrm{static}} = \lim_{\beta_{\mathrm{p}} \to 0} M_y = \frac{4\pi D(1 + a^2/R^2)}{1 - a^2/R^2 + (1 + a^2/R^2)\log(a/R)} \Psi, \tag{A 10}$$

respectively. Calling $\epsilon = a/R$, we finally derive the conditions (2.4) and (2.5), with the signs chosen in accordance with the adopted convention for the bending moments and axial force in the beam.

References

1. Slepyan LI. 2002 *Models and phenomena in fracture mechanics*. Berlin, Germany: Springer.
2. Slepyan LI. 1981 Dynamics of a crack in a lattice. *Sov. Phys. Dokl.* **26**, 538–540.
3. Slepyan LI. 2015 On the energy partition in oscillations and waves. *Proc. R. Soc. A* **471**, 20140838. (doi:10.1098/rspa.2014.0838)
4. Slepyan LI, Movchan AB, Mishuris GS. 2010 Crack in a lattice waveguide. *Int. J. Fract.* **162**, 91–106. (doi:10.1007/s10704-009-9389-5)
5. Nieves MJ, Mishuris GS, Slepyan LI. 2016 Analysis of dynamic damage propagation in discrete beam structures. *Int. J. Solids Struct.* **97–98**, 699–713. (doi:10.1016/j.ijsolstr.2016.02.033)
6. Nieves MJ, Mishuris GS, Slepyan LI. 2017 Transient wave in a transformable periodic flexural structure. *Int. J. Solids Struct.* **112**, 185–208. (doi:10.1016/j.ijsolstr.2016.11.012)
7. Ayzenberg-Stepanenko M, Slepyan LI. 2008 Resonant-frequency primitive waveforms and star waves in lattices. *J. Sound Vib.* **313**, 812–821. (doi:10.1016/j.jsv.2007.11.047)
8. Osharovich G, Ayzenberg-Stepanenko M, Tsareva O. 2010 Wave propagation in elastic lattices subjected to a local harmonic loading. II. Two-dimensional problems. *Cont. Mech. Thermodyn.* **22**, 599–616. (doi:10.1007/s00161-010-0164-7)
9. D'Eleuterio GMT, Hughes PC. 1984 Dynamics of gyroelastic continua. *J. Appl. Mech.* **51**, 415–422. (doi:10.1115/1.3167634)
10. Hughes PC, D'Eleuterio GMT. 1986 Modal parameter analysis of gyroelastic continua. *J. Appl. Mech.* **53**, 918–924. (doi:10.1115/1.3171881)
11. D'Eleuterio GMT. 1988 On the theory of gyroelasticity. *J. Appl. Mech.* **55**, 488–489. (doi:10.1115/1.3173705)
12. Yamanaka K, Heppler GR, Huseyin K. 1996 Stability of gyroelastic beams. *AIAA J.* **34**, 1270–1278. (doi:10.2514/3.13223)
13. Prall D, Lakes RS. 1997 Properties of a chiral honeycomb with a Poisson's ratio of −1. *Int. J. Mech. Sci.* **39**, 305–314. (doi:10.1016/S0020-7403(96)00025-2)
14. Tee KF, Spadoni A, Scarpa F, Ruzzene M. 2010 Wave propagation in auxetic tetrachiral honeycombs. *J. Vib. Acoust.* **132**, 031007. (doi:10.1115/1.4000785)
15. Bigoni D, Guenneau S, Movchan AB, Brun M. 2013 Elastic metamaterials with inertial locally resonant structures: application to lensing and localization. *Phys. Rev. B* **87**, 174343. (doi:10.1103/PhysRevB.87.174303)
16. Zhu R, Liu XN, Hu GK, Sun CT, Huang GL. 2014 A chiral elastic metamaterial beam for broadband vibration suppression. *J. Sound Vib.* **333**, 2759–2773. (doi:10.1016/j.jsv.2014.01.009)
17. Tallarico D, Movchan NV, Movchan AB, Colquitt DJ. 2017 Tilted resonators in a triangular elastic lattice: Chirality, Bloch waves and negative refraction. *J. Mech. Phys. Solids* **103**, 236–256. (doi:10.1016/j.jmps.2017.03.007)
18. Tallarico D, Trevisan A, Movchan NV, Movchan AB. 2017 Edge waves and localization in lattices containing tilted resonators. *Front. Mater.* **4**, 16. (doi:10.3389/fmats.2017.00016)
19. Carta G, Nieves MJ, Jones IS, Movchan NV, Movchan AB. 2018 Elastic chiral waveguides with gyro-hinges. *Quart. J. Mech. Appl. Math.* **71**, 157–185. (doi:10.1093/qjmam/hby001)
20. Nieves MJ, Carta G, Jones IS, Movchan AB, Movchan NV. 2018 Vibrations and elastic waves in chiral multi-structures. *J. Mech. Phys. Solids* **121**, 387–408. (doi:10.1016/j.jmps.2018.07.020)
21. Ziegler H. 1977 *Principles of structural stability*, 2nd edn. Basel, Switzerland: Springer.
22. Brun M, Jones IS, Movchan AB. 2012 Vortex-type elastic structured media and dynamic shielding. *Proc. R. Soc. A* **468**, 3027–3046. (doi:10.1098/rspa.2012.0165)
23. Carta G, Brun M, Movchan AB, Movchan NV, Jones IS. 2014 Dispersion properties of vortex-type monatomic lattices. *Int. J. Solids Struct.* **51**, 2213–2225. (doi:10.1016/j.ijsolstr.2014.02.026)
24. Carta G, Jones IS, Movchan NV, Movchan AB, Nieves MJ. 2017 'Deflecting elastic prism' and unidirectional localisation for waves in chiral elastic systems. *Sci. Rep.* **7**, 26. (doi:10.1038/s41598-017-00054-6)
25. Carta G, Jones IS, Movchan NV, Movchan AB, Nieves MJ. 2017 Gyro-elastic beams for the vibration reduction of long flexural systems. *Proc. R. Soc. A* **473**, 20170136. (doi:10.1098/rspa.2017.0136)
26. Carta G, Nieves MJ, Jones IS, Movchan NV, Movchan AB. 2019 Flexural vibration systems with gyroscopic spinners. *Phil. Trans. R. Soc. A* **377**, 20190154. (doi:10.1098/rsta.2019.0154)

27. Carta G, Colquitt DJ, Movchan AB, Movchan NV, Jones IS. Submitted. Chiral flexural waves in structured plates: directional localisation and control. *J. Mech. Phys. Solids*.
28. Haslinger SG, Craster RV, Movchan AB, Movchan NV, Jones IS. 2016 Dynamic interfacial trapping of flexural waves in structured plates. *Proc. R. Soc. A* **472**, 20150568. (doi:10.1098/rspa.2015.0658)
29. Haslinger SG, Movchan NV, Movchan AB, Jones IS, Craster RV. 2017 Controlling flexural waves in semi-infinite platonic crystals with resonator-type scatterers. *Q. J. Mech. Appl. Math.* **70**, 216–247. (doi:10.1093/qjmam/hbx005)
30. Raghu S, Haldane FDM. 2008 Analogs of quantum-Hall-effect edge states in photonic crystals. *Phys. Rev. A* **78**, 033834. (doi:10.1103/PhysRevA.78.033834)
31. Wang Z, Chong YD, Joannopoulos JD, Soljačić M. 2008 Reflection-free one-way edge modes in a gyromagnetic photonic crystal. *Phys. Rev. Lett.* **100**, 013905. (doi:10.1103/PhysRevLett.100.013905)
32. He C, Chen XL, Lu MH, Li XF, Wan WW, Qian XS, Yin RC, Chen YF. 2010 Left-handed and right-handed one-way edge modes in a gyromagnetic photonic crystal. *J. Appl. Phys.* **107**, 123117. (doi:10.1063/1.3374470)
33. Khanikaev AB, Mousavi SH, Tse WK, Kargarian M, MacDonald AH, Shvets G. 2013 Photonic topological insulators. *Nat. Mater.* **12**, 233–239. (doi:10.1038/nmat3520)
34. Gao W, Lawrence M, Yang B, Liu F, Fang F, Béri J, Li J, Zhang S. 2015 Topological photonic phase in chiral hyperbolic metamaterials. *Phys. Rev. Lett.* **114**, 037402. (doi:10.1103/PhysRevLett.114.037402)
35. Pal RK, Ruzzene M. 2017 Edge waves in plates with resonators: an elastic analogue of the quantum valley Hall effect. *New J. Phys.* **19**, 025001. (doi:10.1088/1367-2630/aa56a2)
36. Makwana MP, Craster RV. 2018 Geometrically navigating topological platonic modes around gentle and sharp bends. *Phys. Rev. B* **98**, 184105. (doi:10.1103/PhysRevB.98.184105)
37. Makwana MP, Craster RV. 2018 Designing multi-directional energy-splitters and topological valley supernetworks. *Phys. Rev. B* **98**, 235125. (doi:10.1103/PhysRevB.98.235125)
38. Chaplain GJ, Makwana MP, Craster RV. 2019 Rayleigh-Bloch, topological edge and interface waves for structured elastic plates. *Wave Motion* **86**, 162–174. (doi:10.1016/j.wavemoti.2019.01.008)
39. Wang P, Lu L, Bertoldi K. 2015 Topological phononic crystals with one-way elastic edge waves. *Phys. Rev. Lett.* **115**, 104302. (doi:10.1103/PhysRevLett.115.104302)
40. Nash LM, Kleckner D, Read A, Vitelli V, Turner AM, Irvine WTM. 2015 Topological mechanics of gyroscopic metamaterials. *Proc. Natl Acad. Sci. USA* **112**, 14 495–14 500. (doi:10.1073/pnas.1507413112)
41. Garau M, Carta G, Nieves MJ, Jones IS, Movchan NV, Movchan AB. 2018 Interfacial waveforms in chiral lattices with gyroscopic spinners. *Proc. R. Soc. A* **474**, 20180132. (doi:10.1098/rspa.2018.0132)
42. Zheng L-Y, Teocharis G, Tournat V, Gusev V. 2018 Quasitopological rotational waves in mechanical granular graphene. *Phys. Rev. B* **97**, 060101. (doi:10.1103/PhysRevB.97.060101)
43. Süsstrunk R, Huber SD. 2015 Observation of phononic helical edge states in a mechanical topological insulator. *Science* **349**, 47–50. (doi:10.1126/science.aab0239)
44. Piccolroaz A, Movchan AB, Cabras L. 2017 Dispersion degeneracies and standing modes in flexural waves supported by Rayleigh beam structures. *Int. J. Solids Struct.* **109**, 152–165. (doi:10.1016/j.ijsolstr.2017.01.017)
45. Piccolroaz A, Movchan AB, Cabras L. 2017 Rotational inertia interface in a dynamic lattice of flexural beams. *Int. J. Solids Struct.* **112**, 43–53. (doi:10.1016/j.ijsolstr.2017.02.023)
46. Bordiga G, Cabras L, Bigoni D, Piccolroaz A. 2019 Free and forced wave propagation in a Rayleigh-beam grid: Flat bands, Dirac cones, and vibration localization vs isotropization. *Int. J. Solids Struct.* **161**, 64–81. (doi:10.1016/j.ijsolstr.2018.11.007)
47. Bordiga G, Cabras L, Piccolroaz A, Bigoni D. 2019 Prestress tuning of negative refraction and wave channeling from flexural sources. *Appl. Phys. Lett.* **114**, 5084258. (doi:10.1063/1.5084258)
48. Haslinger SG, Movchan NV, Movchan AB, McPhedran RC. 2012 Transmission, trapping and filtering of waves in periodically constrained elastic plates. *Proc. R. Soc. A* **468**, 74–93. (doi:10.1098/rspa.2011.0318)
49. Haslinger SG, Jones IS, Movchan NV, Movchan AB. 2018 Localisation in semi-infinite herringbone waveguides. *Proc. R. Soc. A* **474**, 20170590. (doi:10.1098/rspa.2017.0590)

50. Morvaridi M, Carta G, Brun M. 2018 Platonic crystal with low-frequency locally-resonant spiral structures: wave trapping, transmission amplification, shielding and edge waves. *J. Mech. Phys. Solids* **121**, 496–516. (doi:10.1016/j.jmps.2018.08.017)
51. Movchan AB, McPhedran RC, Carta G, Craster RV. 2019 Platonic localisation: one ring to bind them. *Arch. Appl. Mech.* **89**, 521–533. (doi:10.1007/s00419-018-1465-8)
52. Cai L-W, Hambric SA. 2016 Movable rigid scatterer model for flexural wave scattering on thin plates. *J. Vib. Acoust.* **138**, 031016. (doi:10.1115/1.4033060)